Zentrum für Technomathematik

Fachbereich 3 – Mathematik und Informatik

Adaptive Finite Element Models Applied to the Laser Welding Problem

Jonathan Montalvo-Urquizo Zafer Akbay
Alfred Schmidt Thomas Pretorius

Report 08–03

Berichte aus der Technomathematik

Report 08–03 **Oktober 2008**

Adaptive Finite Element Models Applied to the Laser Welding Problem

J. Montalvo-Urquizo[a,*], Z. Akbay[b], A. Schmidt[a], T. Pretorius[b]

[a] *Zentrum für Technomathematik, Fachbereich 3, University of Bremen, Germany*
[b] *Bremer Institut für Angewandte Strahltechnik, Bremen, Germany*

Abstract

We present a coupled simulation of the thermal and mechanical problems of the laser welding process. The thermal simulation is based on an energy balance idea for the construction of the keyhole and its further use as the heat source shape. The mechanical model includes the thermo-elasto-plastic solution, required for the residual state computation.

The coupled model is described and some results of their implementation are presented. The implementation was done using the Adaptive-FEM Toolbox ALBERTA, making use of a posteriori error estimation for the proper adaption of the mesh with respect to the moving heat source. Further, the simulated process is shown to be in accordance with experimental results obtained with the same process parameters.

Key words: welding, laser welding, aluminum alloys, plastic deformation, residual stress
PACS: 44.05.+e, 46.35.+z, 81.20.Vj

1. Introduction

As one of the most modern welding techniques, deep penetration laser welding has strongly attracted the attention of the production and research communities since the last decade. The research directions, guided by the industrial needs, have tried to analyze and numerically simulate the welding process based in

* Corresponding author
Email addresses: montalvo@math.uni-bremen.de (J. Montalvo-Urquizo), zafer@math.uni-bremen.de (Z. Akbay), schmidt@math.uni-bremen.de (A. Schmidt), pretorius@bias.de (T. Pretorius)

models already existent for other welding processes. However, in many of these simulations the main characteristic of the deep penetration welding is underestimated and the existence of a vapor channel, or keyhole, is not considered.

The main difficulties for the keyhole consideration arise from its own dimensional size, being a very narrow and long channel created in the laser beam direction and shifted along the welding line in the material. Typical sizes of its radius are in the order of 0.1mm, while its length is on the order of several millimeters.

On the other hand, part of the interesting features of the laser welding techniques are their high welding speeds. This leads to a disputed situation because a simulation must contain a high refinement to simulate the motion of the tiny keyhole, and it must be fast to allow the computation of the large piece of welded material.

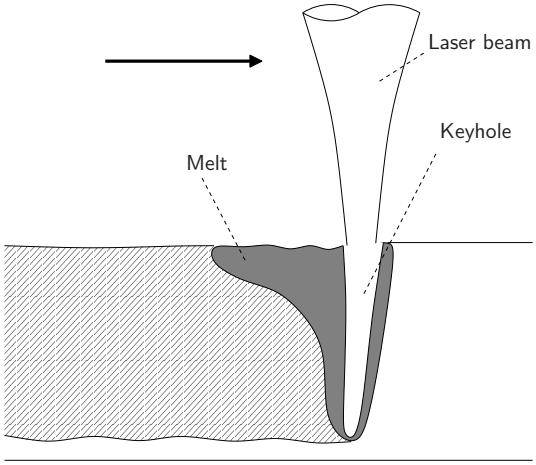

Figure 1: Schematic view of a laser welding process. The laser beam moves from left to right melting the material and the weld seam is created after resolidification.

To overcome these difficulties, we present here a simulation based on Adaptive Finite Element Methods (AFEM). This implementation considers the thermal evolution in the material piece, together with a mechanical model for the computation of elastic and elasto-plastic deformations, strains and stresses.

The thermal and mechanical models are presented in Sections 2 and 3, respectively. Section 4 contains the details about the implemented simulation and Section 5 presents some numerical results together with experimental comparisons. Finally, Section 6 summarizes the main ideas of this work and introduce some further research needs.

2. Thermal problem

The welding process is based in the melting and solidification of material around the welding line. In order to obtain the heat necessary for the material melting to occur, a focused laser beam is used as heat source.

After a very short instability period, a narrow and long hole is formed in the material and, if the laser beam is translated along the welding line, this hole accompanies its motion (see Figure 1). Models for the keyhole formation exist in many different levels of complexity, going from simple line sources (e.g. [1, 2]) to rather complex models which compute accurate keyhole shapes, as the ones presented by [3, 4, 5, 6, 7]. The problem with the first ones is that they neglect the keyhole existence, while the second ones need an extremely expensive computational work.

Within this work, we take a keyhole model based on the energy balance idea, as presented in [8, 9]. The main advantage of this idea is the possibility of computing very fast the rough shape of the keyhole. This keyhole shape can then be used as the heat source, assuming that the temperature inside the keyhole is equal to the evaporation temperature of the material.

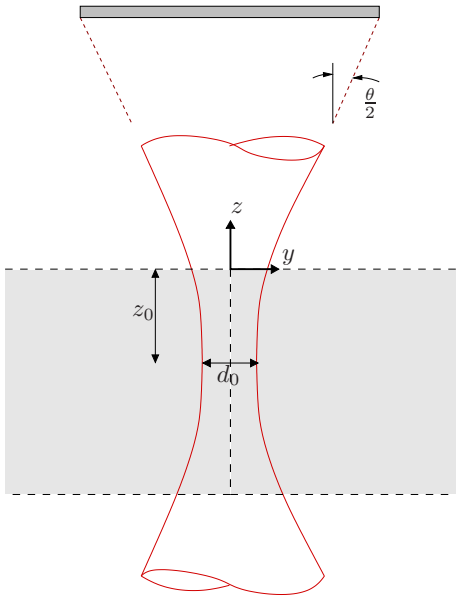

Figure 2: Schematic laser beam focused inside the material piece.

The keyhole frontal shape can be obtained comparing the energy used to evaporate material with the energy contained in the laser beam in absence of material.

Without loss of generality, we assume that the laser beam is oriented in the vertical direction, and is moving along the x-direction. Now, if we consider a y coordinate close to the beam center, the penetration of the beam into the material can be obtained (as in [9]) using the equation

$$\frac{vQ}{d_0}\int_0^z \sqrt{d_0^2+\theta^2(s-z_0)^2}\,dz = \int_{-a}^{a} \frac{\eta P}{\pi\left(\frac{d_0^2}{4}\right)}dx, \tag{1}$$

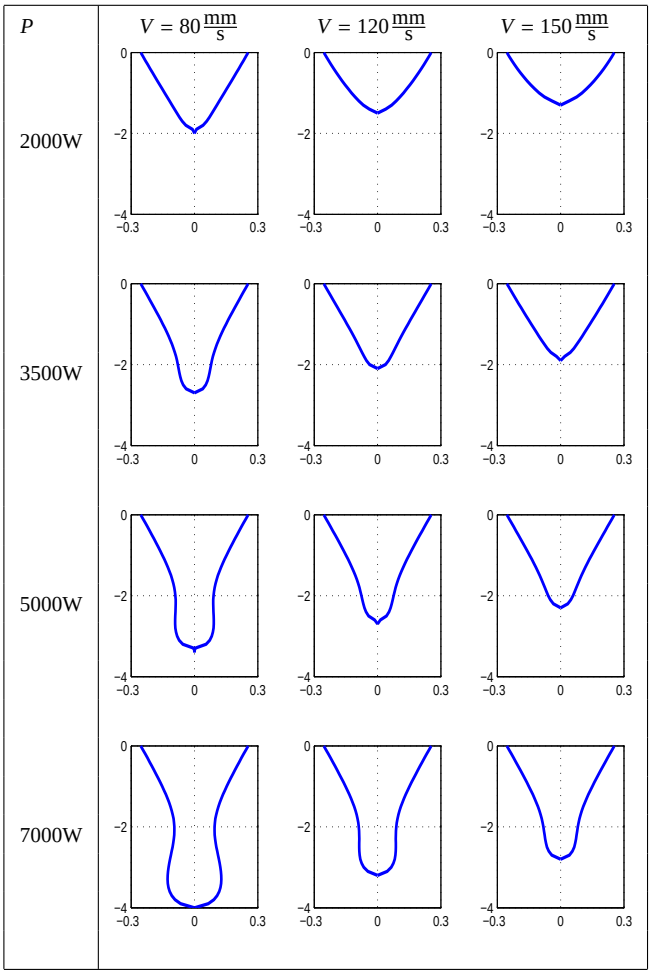

Figure 3: Computed keyhole shapes for different values of laser power and welding velocity.

$$a = \sqrt{\frac{d_0^2}{4} - y^2}, \tag{2}$$

where v is the welding velocity, Q is the energy used for evaporating a unit of material volume and the laser beam is characterized by the waist diameter d_0, the divergence angle θ, and the focus vertical position z_0 (see Figure 2). Here, we consider a laser beam of constant distribution, as can be observed from the simple expression inside the integral of the right hand side in equation (1). For a Gaussian beam, the corresponding distribution must be substituted inside this integral.

After some simple steps, the last equation can be transformed into

$$vQ \int_0^z \sqrt{d_0^2 + \theta^2 (s - z_0)^2}\, dz \quad = \quad \frac{4\eta P \sqrt{d_0^2 - 4y^2}}{\pi d_0} \tag{3}$$

and this equation can be solved to get the pairs (y, z) describing the frontal shape of the keyhole.

Figure 3 shows the different keyhole shapes obtained for different values of the laser beam power P and velocity v with a laser beam focused at $z_0 = -2.0$mm (slightly inside the material), and the other parameters taken as $Q = 40\text{J/m}^3$, $d_0 = 0.6$mm, $\theta = 5.98°$, and $\eta = 0.8$.

As one would expect, the keyhole size increases when using higher values of laser power, and decreases when using higher welding velocities. Note also that for keyhole shapes large enough, the beam waist at $z = -2.0$mm is maintained.

For the welding simulation, we consider the domain Ω describing the material piece for a butt weld and a time-dependent keyhole subdomain for which the temperature θ is set at the evaporation temperature value, it is

$$\frac{\partial \theta}{\partial t} - \frac{\partial}{\partial x}\left(\kappa(\theta)\frac{\partial \theta}{\partial x}\right) = \frac{f(x)}{\rho C_e(\theta)} \quad \text{in } \tilde{\Omega} \times (0, T), \tag{4}$$

$$\kappa(\theta)\frac{\partial \theta}{\partial n} = \delta_{air}(\theta - \theta_0) \quad \text{on } \partial\Omega \times (0, T), \tag{5}$$

$$\theta = \theta_0 \quad \text{in } \tilde{\Omega} \times \{0\}, \tag{6}$$

$$\theta = \theta_v \quad \text{in } \Omega \backslash \tilde{\Omega}. \tag{7}$$

In this modified heat equation the heat diffusivity κ and the specific heat capacity C_e are considered temperature dependent, as their changing values for different temperatures play an important role in the welding simulation due to

the intrinsic nature of large temperature variations. The values θ_0 and θ_v correspond to the room and evaporation temperatures, ρ is the density, and δ_{air} is the heat transfer coefficient between the material piece and the air around it.

A direct computation of the temperature on the keyhole subdomain $\Omega\backslash\tilde{\Omega}$ is difficult to perform, due to its very small size and fast motion. For this, a much better idea is to assume evaporation temperature inside this subdomain and perform an adaptive computation in the rest of the domain as in equation (4).

We make use of the already existent a posteriori error estimators for the heat equation, see e. g. [10] and the references therein. The use of an adaptive method allows the fine computation in the moving region of the keyhole, while a coarser computation is done for the rest of the domain.

3. Mechanical problem

The mechanical effects of the welding process are as important as the thermal ones, being of special interest the deformations that occur in the material as it is drastically heated and cooled.

In the case of thermal forces of moderate size, the mechanical equations to solve are the ones of the thermoelasticity, given by

$$-\mathrm{div}(\sigma) = f_\sigma \qquad \text{in } \Omega \times (0,T), \tag{8}$$

$$u = \mathbf{0} \qquad \text{on } \Gamma_0 \times (0,T), \tag{9}$$

$$n \cdot \sigma(\mathbf{u}) = \mathbf{0} \qquad \text{on } \Gamma_N \times (0,T). \tag{10}$$

with $\mathbf{u} \in \mathbb{R}^3$ denoting the displacement field, and with ε and σ being the strain and stress tensors in $\mathbb{R}^{3\times3}$, it is

$$\varepsilon(\mathbf{u}) = \frac{1}{2}\left(\nabla\mathbf{u} + \nabla\mathbf{u}^T\right), \tag{11}$$

$$\sigma = \lambda \mathrm{tr}(\varepsilon) I_3 + 2\mu\varepsilon - 3B\alpha^\theta(\theta - \theta_0) I_3, \tag{12}$$

where λ and μ denote the Lamé constants, α^θ is the thermal expansion coeffcient, and B is the corresponding bulk modulus

$$B = \lambda + \frac{2}{3}\mu. \tag{13}$$

Solving equations (4)-(7) together with equations (8)-(12) in every time step, would give a solution for the thermoelastic problem.

However, the welding process we are interested in, produces very large temperature gradients. These gradients are then traduced in large strains and in plastic stresses and deformations, for which an elastic approach is not enough (see e.g. [11, 12, 13] for a complete explanation of the mechanical behavior during welding).

In order to handle the plastic deformations together with the thermal computations, we make use of the radial return mapping proposed in [14] for elasto-plastic problems. For the case of a thermo-elasto-plastic problem with isotropic linear hardening, the radial return mapping with von Mises flow rule can be written as the following algorithm (see e.g. [15]):

Radial Return Mapping with Linear Isotropic Hardening and von Mises Flow Rule

1. Define the trial state as
$$\mathbf{s}_{n+1}^{\text{trial}} = 2\mu\,(\text{dev}(\varepsilon) - \varepsilon^p)$$
2. Check the yield condition using the von Mises flow function
$$\bar{f}_{n+1} = \left\|\mathbf{s}_{n+1}^{\text{trial}}\right\| - \sqrt{\tfrac{2}{3}}\hat{K}(\alpha_n)$$
If $\bar{f}_{n+1} \leq 0$, **then** go to Step 3,
else, go to Step 4.
3. Point inside the allowable stresses.
Set
$$\begin{aligned}\alpha_{n+1} &= \alpha_n,\\ \varepsilon_{n+1}^p &= \varepsilon_n^p,\\ \sigma_{n+1} &= \lambda\text{tr}(\varepsilon^e)I_3 + 2\mu\varepsilon^e\\ &\quad -3B\alpha^\theta(\theta-\theta_0)I_3,\end{aligned}$$
Go to Step 6.
4. Compute the normal direction
$$\mathbf{n}_{n+1} = \frac{\mathbf{s}_{n+1}^{\text{trial}}}{\left\|\mathbf{s}_{n+1}^{\text{trial}}\right\|}.$$
Compute the new $\Delta\gamma$ as
$$\Delta\gamma = \frac{\left\|\mathbf{s}_{n+1}^{\text{trial}}\right\| - \sqrt{2/3}(\sigma_Y + K\alpha_n)}{2\mu + \frac{2}{3}K}.$$
Update the equivalent plastic strain
$$\alpha_{n+1} = \alpha_n + \Delta\gamma.$$
5. Update the values plastic strain and stress as
$$\begin{aligned}\varepsilon_{n+1}^p &= \varepsilon_n^p + \Delta\gamma\eta_{n+1},\\ \sigma_{n+1} &= \lambda\text{tr}(\varepsilon^e)I_3 + 2\mu\varepsilon^e\\ &\quad -3B\alpha^\theta(\theta-\theta_0)I_3 - 2\mu\left(\varepsilon_n^p + \Delta\gamma\eta\right).\end{aligned}$$
6. Exit

This is an algorithm of the general predictor-corrector type ([14, 16]) in which the state of strain and plastic strain are computed such that the stress never lays outside the space of allowable stresses under the corresponding yield value σ_Y.

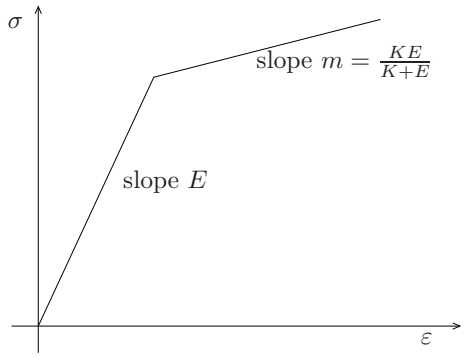

Figure 4: Strain-stress diagram for a material with linear elastic and linear plastic behavior. The plastic modulus is obtained from the slope *m*.

The linear hardening rule used in Step 2 is

$$\hat{K}(\alpha) = \sigma_Y + K\alpha, \tag{14}$$

where K is the plastic modulus of the material obtained from an approximated material behavior as the one in Figure 4

Other more general models for computational plasticity can be found in e.g. [14, 17, 18, 19], where nonlinear models are presente and also models including kinematic hardening are considered.

According to [20, 2], for all the welding processes based on the motion of a heat source, the mechanical behavior experienced in the material can be schematically described using the diagram in Figure 5. In this figure, several states of the mechanical effects are represented for different positions around the welding point. The dashed line indicates the positions of maximum temperature along a longitudinal cut on the weld. This line separates the zones of compression and shrinkage, which are obtained as result of a negative and a positive gradients in the longitudinal (or welding) direction.

From the well established computational welding mechanics theories, it is known that there is a value below the melting point at which the mechanical behavior is affected by viscoplastic phenomena.

The use of material properties which are cut off at this value is known to be a solution to the lack of viscoplastic computations, allowing the use of a

simple elasto-plastic computation for the materials at high temperatures (see e.g. [15, 2]).

For Steels, [20] mentions that proper cut-off temperatures are found around two thirds of the melting temperature measured in Kelvin, i.e. $\theta_c \approx 1200°C$. For aluminum, our experimental tests have shown that values of $\theta_c \approx 600°C$ are well suited.

If one considers a small piece of material close to the welding line, the experienced mechanical effects ilustrated in Figure 5 are:

- After being far enough from the heat source, the metal is suddenly heated up and the thermal expansion from points around the heat source generate forces from left to right and compressive effects take place, being first of elastic and later of elastoplastic nature. The sign of stress in this compressive zone is negative.

- In a small region between the line of maximum temperatures and the shrinkage region, the temperature does not change drastically and the small cooling releases elastically the compressive forces from the previous stage.

- Inside the shrinkage region, the material pieces are cooled down very fast and this cooling causes a new plastic deformation of positive sign.

  The creation of the new plastic effects is of much smaller size as the compressive part. However, this effect happens during a much longer period of

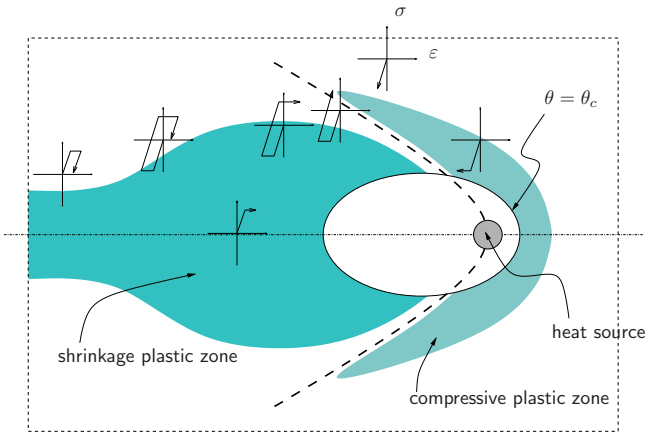

Figure 5: Plastic zones of compressive and tensile type during the creation of a but-weld. The dashed line corresponds to the set of maximum temperatures along a horizontal line (longitudinal direction) in the figure. Modified from [2].

time and, in the end, the sum of the effects can be expected to be of high tensile nature.

As a result, after the weld is finished and the material has a homogeneous temperature, the plastic strains created during the welding process remain. In the final state, after the welding and cooling processes are finished, the material piece contains not only residual strain, but also plastic deformations and their corresponding residual stresses.

4. Simulation setting

The thermal and mechanical models from the previous sections have been implemented in the AFEM Toolbox ALBERTA (see [10]) and used to simulate a butt-weld in which two pieces of size 100mm $\times$ 65mm $\times$ 3mm are welded as depicted in Figure 6, where also the weld seam and the starting and ending points are indicated.

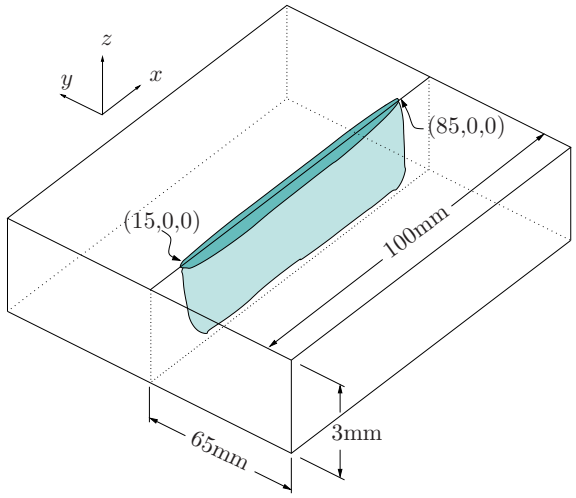

Figure 6: Material piece geometry with start and end points for the butt-weld.

The thermal computations include the a posteriori error estimation for the thermal problem. This error estimation allows a mesh adaption for the better definition of the computations around the dynamic position of the keyhole subdomain $\Omega \backslash \tilde{\Omega}$ from equations (4)-(7). For every time-step, the computations assume that inside this subdomain the temperature equals the evaporation temperature. A

similar error estimation technique for the mechanical problem was not considered.

The considered material piece has a full size of 100mm $\times$ 130mm $\times$ 3mm and is discretized by an initial mesh with 36000 elements and 8364 DOFs.

This mesh was constructed in two steps, first dividing the geometry in $50 \times 40 \times 3$ cubes for the x, y, and z directions, and then dividing each of these cubes into six tetrahedra.

Material: Aluminum alloy AA6082-T6	
Evaporation energy	$40\,\mathrm{Ws/mm^3}$
Melting temperature	$650\,^\circ\mathrm{C}$
Evaporation temperature	$2600\,^\circ\mathrm{C}$
Density	$\rho = 2.7 \times 10^{-6}\,\mathrm{g/mm^3}$
Specific heat capacity*	$C_e = 800\,\mathrm{J/gK}$
Thermal conductivity*	$k = 0.16\,\mathrm{W/mmK}$
Heat-transfer coeff. (air)*	$\delta = 2.5 \times 10^{-6}\ \mathrm{W/mm^2K}$
Thermal expansion coeff.*	$\alpha^\theta = 24 \times 10^{-6}/\mathrm{K}$
Poisson ratio	$\nu = 0.33$
Young modulus*	$E = 72 \times 10^3\,\mathrm{MPa}$
Yield stress*	$280\,\mathrm{MPa}$
Plastic modulus	$K = 1380\mathrm{MPa}$
Cut-off temperature	$600\,^\circ\mathrm{C}$

Table 1: Material properties at room temperature for the aluminum alloy AA6082-T6. The stars indicate that the material properties were considered temperature dependent, with the values in [15].

Distribution type	Constant
Focal length	$f = 450\,\mathrm{mm}$
Focal diameter	$d_0 = 0.06\,\mathrm{mm}$
Last mirror diameter	$D = 47\,\mathrm{mm}$
Focal height	$z_0 = -2\,\mathrm{mm}$
Laser efficiency	$\eta = 0.85$

Table 2: Laser beam parameters fixed for all simulations.

Table 1 shows the material parameters used in the simulation for the room temperature of 25°C. For the temperature dependent parameters in the thermal an mechanical equations, the values are the ones in [15].

The laser beam parameters used for the simulations are the ones shown in Table 2.

The implemented models also include the measurement of the meltpools during the welding time, allowing the measurement of the resulting weld seam width w and height h. Further, the mechanical computations are used to get the deformation 300 seconds after the welding is finished.

After this cooling period ($t_{cool} = 300$s), the temperature in the welded piece is practically homogeneous, experiencing only small changes due to the heat transfer from the piece into the surrounding air. At this last simulation time, no more plastic deformations can occur and the measurements for the residual displacement and the out-of-plane angle in the material can be performed.

Considering the starting and end points from Figure 6, the total weld length is 70mm, and the corresponding welding time is $t_w = 70\text{mm}/v$, with v denoting the welding velocity. The final simulation time is then $T = t_w + t_{cool}$.

5. Simulation results and comparisons with experiments

Using the models in Sections 2 and 3, and the specifications in Section 4, we present now the results of the simulated weld using the laser power $P = 3000$W and the welding velocity $v = 75$mm/s.

The results of the ALBERTA implementation are presented along with the welding results obtained experimentally.

The experimental welds shown here were obtained using the same conditions as the ones assumed for the simulated welds, with the intention to reproduce the experimental weld using the computational model.

5.1. Thermal results

Once the temperature fields are computed, the isoline of the melting temperature determines the line at which the solid–liquid phase change line is located.

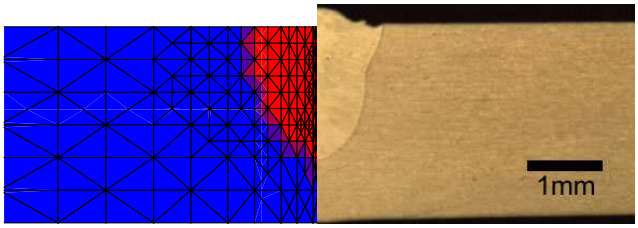

Figure 7: Experimental and simulated meltpool.

Figure 7 shows the meltpool obtained for the simulated and the experimental welds for the specified laser power and velocity.

The simulated meltpool size was computed using the locations of the extreme values of the melting temperature isoline. These measurements of the meltpool give a top width $w = 2.657$ mm and a vertical penetration $h = 1.958$ mm.

For the experimental piece, several samples were welded, giving sizes of the meltpool with top width between 2.06 and 2.15 mm, and height values between 1.92 and 2.30 mm.

It is important to notice, that a direct comparison of the keyhole top radius or penetration is not possible due to the non-available measurements for these dimensions. However, the meltpool dimensions computed using the evaporation temperature of 2600°C inside the moving keyhole result in very similar dimensions for simulated and experimental welds.

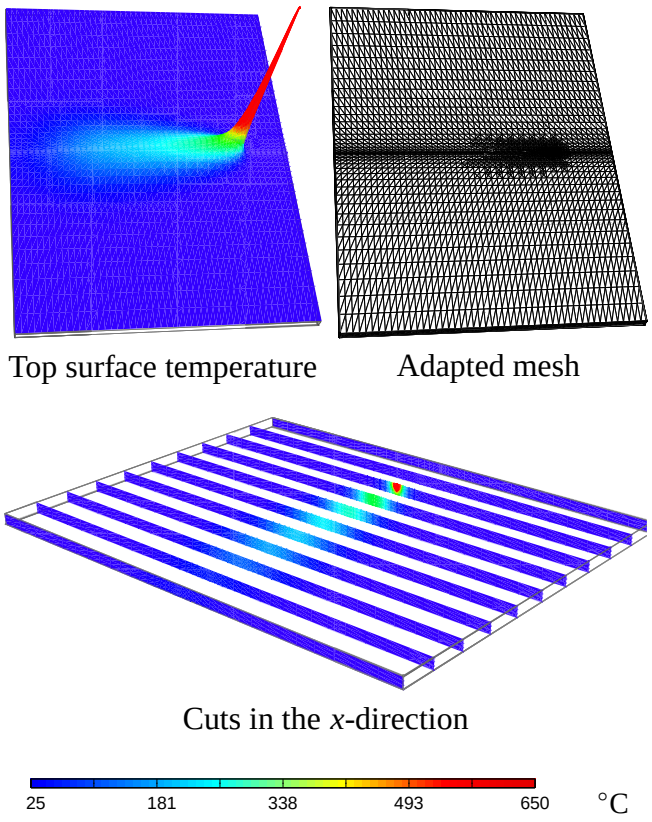

Figure 8: Temperature field and adapted mesh at $t = 0.88$ s. The maximum temperature value is 2600 °C and the colorscale is limited to the temperatures below the melting point.

There exist some small discrepancies between simulated and experimental meltpools, but they can be accepted to be part of the non-modelled phenomena taking place in the process, as could be the convection of liquid material.

Another possible source of experimental discrepancies is the fact that slight changes in the focal height z_0 can represent considerable changes in the keyhole formation and the exact experimental realization of this focal height is always subject to some small error.

The temperature values are presented in Figure 8 for the time at which the laser beam is located at $x = 80\,\text{mm}$. The top surface plot and the cuts in the x directions make possible to see the dimensions of the molten area, which has a wider diameter in the longitudinal direction due to the motion of the heat source.

Note that for the plots in Figure 8, the color scale is finished at the melting temperature. However, the temperature field reaches its maximum value of 2600°C at the center of the meltpool, where the keyhole is located.

The shape of the temperature plot on the top surface shows the high gradients in the region inside and close to the meltpool.

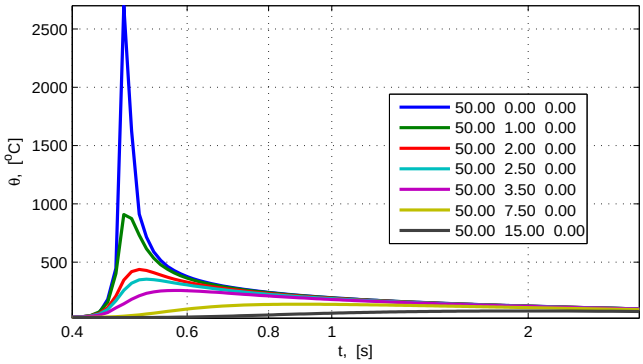

Figure 9: Temperature history for a selection of traversal points on the top surface.

The plots in Figure 9 show the temperature values for a selection of points on the top surface. All the points are located at the longitudinal middle of the plate, and the center of the laser beam reaches this location ($x = 50\,\text{mm}$) at time $t = 0.480\,\text{s}$.

It can be observed that the maximum temperatures are obtained at the moment of the laser beam action if the point locations are close to the welding line. For points away of this line, the maximum values are obtained later. This is a clear effect of the heat diffusion, reaching the neighboring material to the welding line after some affection time. The set of these maximum temperatures is exactly the set depicted as a dashed line in Figure 5.

The meshes presented in Figure 10 show the changes in the mesh for different times of the simulation. In this way, the adaptive process based in the thermal error estimation makes possible an accurate approximation of the thermal process at the time-dependent laser beam location. For a region in the material where the weld already took place, the refinement is gradually decreased and the mesh tends to be coarsened as the time advances.

It is necessary to mention that all meshes have a predefined refinement area close to the region where the weld line is located. This is done in order to avoid an excessive coarsening of elements in this region during the cooling time, which would lead to a poor approximation of the mechanical computations.

Independently of this predefined refinement in the mesh, the obtained element

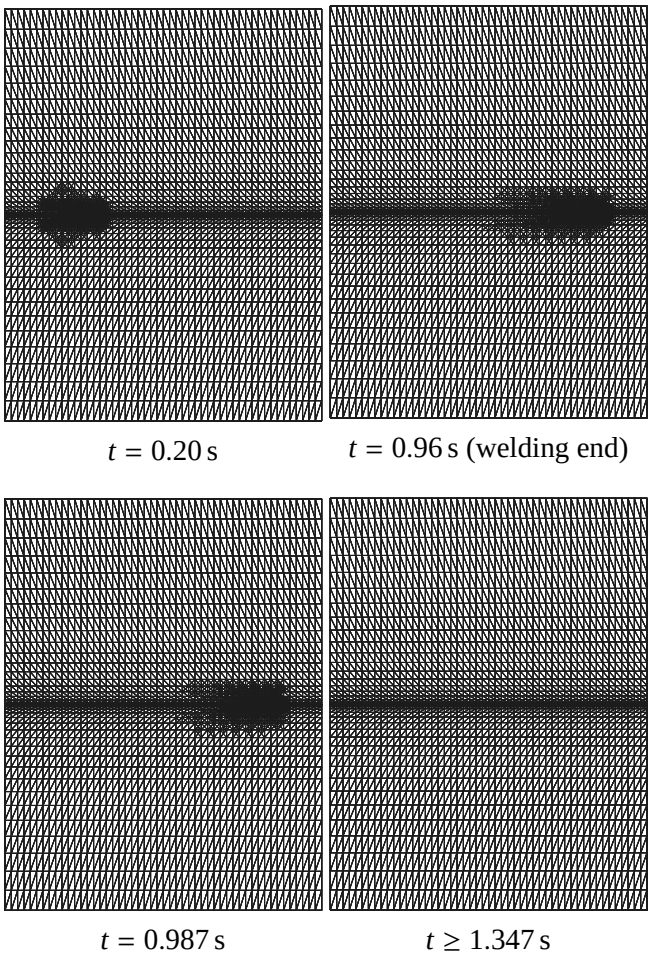

Figure 10: Top view of the adapted meshes at different times.

sizes obtained with the error estimation at the points around the keyhole position are much smaller than this initial refinement size.

For this simulation, the system reaches a maximum of degrees of freedom at the last welding time step, i.e. at $t = 0.96$ s. After this, the mesh returns very fast to its minimal configuration, which is reached at the time $t = 1.347$ s.

Figure 11 shows the evolution of the number of degrees of freedom used for the adapted mesh for every computed time step. The maximum of 21295 DOFs is reached at the end of the welding time, while the original mesh size with 8364 DOFs corresponds to the final welding time and the cooling times.

It is interesting to observe how the amount of degrees of freedom (and hence the discrete system and the computation time) is strongly reduced at the moment when the weld is finished and the keyhole disappears.

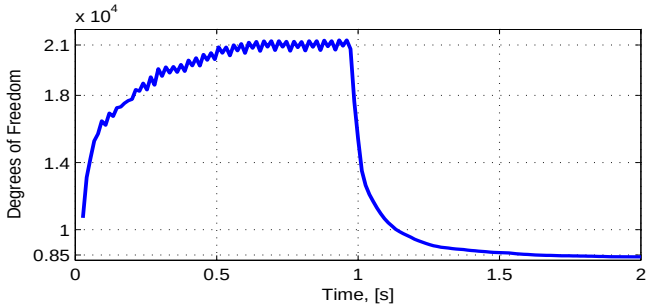

Figure 11: Degrees of freedom evolution for the first two simulated seconds (after this time, the mesh has the original size of 8364 DOFs).

5.2. Mechanical results

For the mechanical results, we are mainly interested on analyzing the stress development in the material, and the plastic effects resulting from the fast heating and cooling processes.

Figure 12 shows the residual deformation in the experimental and the simulated pieces (both exaggerated by a factor of 30), where it is possible to observe the out-of-plane angle. For the simulated weld, additional lines show the original size and position of the material piece.

According to the existent knowledge from welding mechanics, the main two reasons for the material to maintain this semi-folded shape are the non-full penetration of the weld and the 'triangular' shape of the melting pool.

These two factors create differences on the plastic strains for the top and bottom of the plates, causing also differences in the amounts of residual plastic

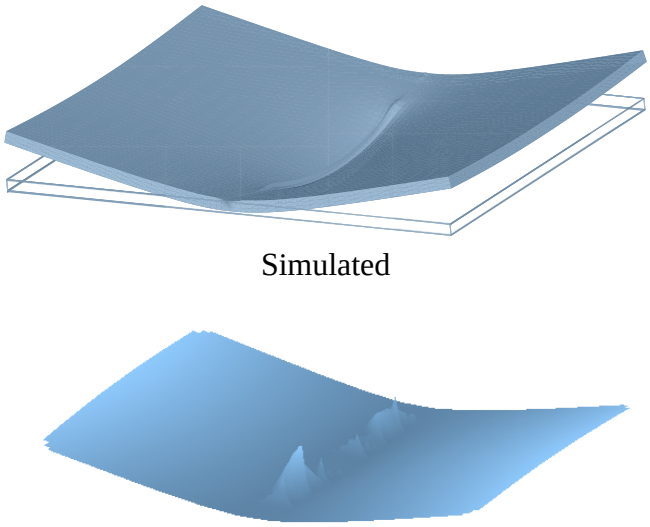

Figure 12: Final deformation of the welded piece. Exaggerated 30 times.

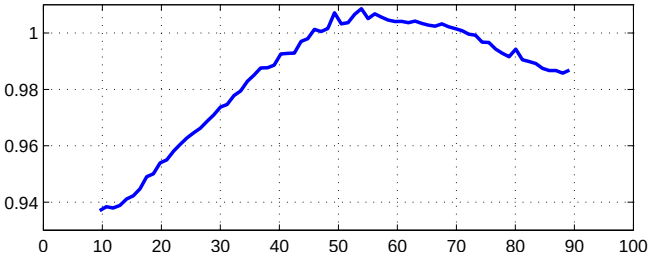

Figure 13: Experimental measurements of the deformation angle for the different x-coordinates.

deformations and stresses and, in the end, bending the plates to equilibrate these internal forces.

The angle of deformation of the simulated weld on the middle of the plate is 0.9520°, while the measured value of the experiment is 1.003°.

The experimental values for the angle deformations are obtained via a post-process measurement of the deformation and, once the deformation is known, a simple geometric relation gives the information about the angle for the different x-coordinates. The obtained measurements are as the ones shown in Figure 13, from where the experimental value mentioned before was taken.

Figure 14 shows the values of the equivalent stress for different z-layers of the material piece at $t = 0.7733$ s. At this time, the laser is still acting on the piece (at

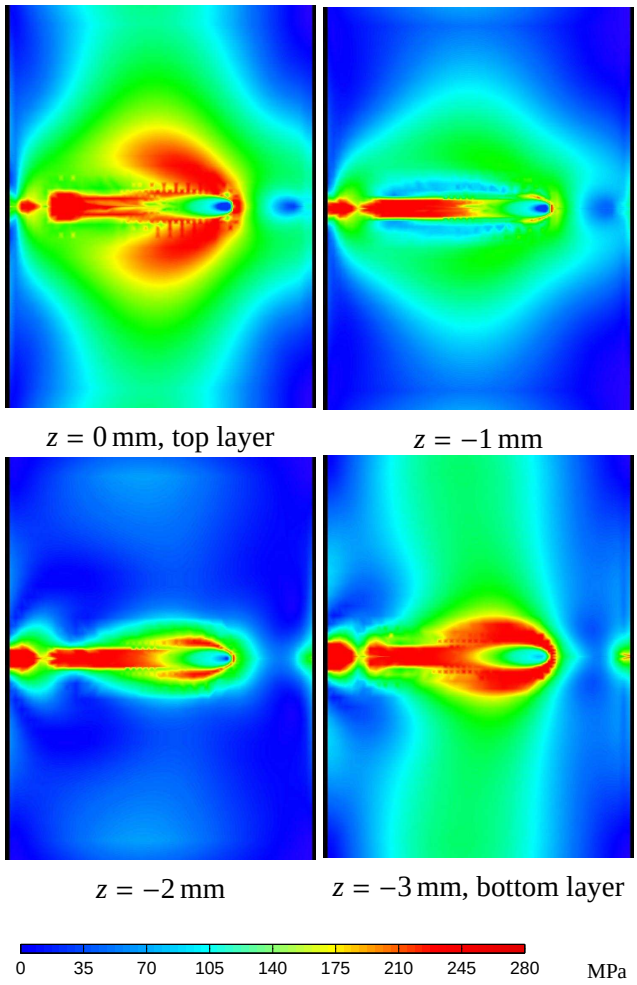

Figure 14: Equivalent stress distribution for different vertical layers of the material piece at $t = 0.7733$ s, when the laser beam is located at $x = 72$ mm.

$x = 72$ mm) and there is a molten region where the weld seam is being formed and most of the mechanical changes can be observed.

At temperatures above the melting point, the equivalent stress is nearly zero. This results in the blue spots located in the molten regions of the top and -1 mm layers in Figure 14. The same spot cannot be found in the bottom layer due to the fact that the weld penetration is slightly less than 2mm and thus the material is solid at this bottom part, being able to contain mechanical stress.

In the same figure, the regions of high compressive stress in front of the welding point can be observed, having similar stress values, but different extensions

and shapes for each of the four layers (compare with Figure 5).

Note that the compressive zone in front of the molten area is very thin, due to the extremely steep temperature field, being almost at room temperature and suddenly heated up when the laser beam reaches a neighboring location.

For regions behind the welding point, the cooling process is taking place, and if the distance to the laser location is large enough, the formation of the final stress can be already observed.

As expected, the thermal vertical difference produces different behaviors of the equivalent residual stress, as can be observed in Figure 15. This plots correspond to the time $T = t_w + t_{cool}$.

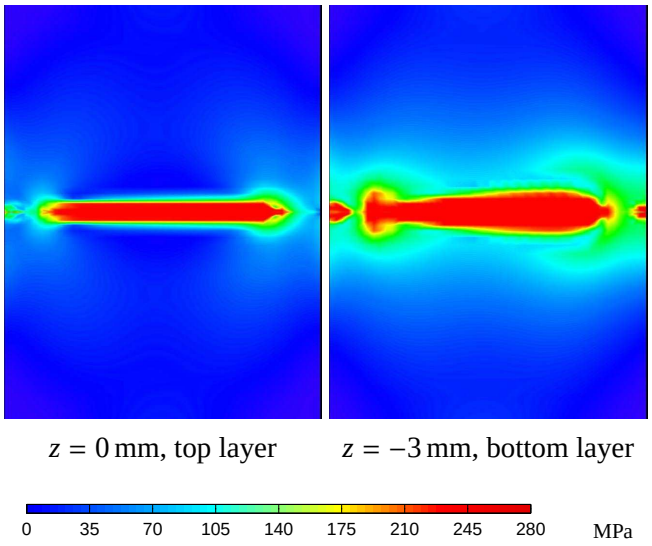

Figure 15: Equivalent stress distribution for the top and bottom of the plate after cooling of the welded piece.

The evolution of the longitudinal strain, plastic strain and stress are presented in Figure 16 for a selection of points over a logarithmic scale of the time interval $[0, 300]$. The points are chosen to belong to the middle of the plate on the vertical direction ($z = -1.5$mm) and have coordinate $x = 30$mm.

The plots show the time marks for the moments at which the laser beam is located at $x = 30$mm ($t = 0.2133$ s), the half time of the welding process ($t = 0.48$ s), and the last time at which the laser beam heats the material ($t = 0.9467$ s). There are several interesting things to observe from Figure 16 as we will mention now.

A common feature of all the components of strain is that they are different from zero at every time step where the temperature distribution is not homogeneous

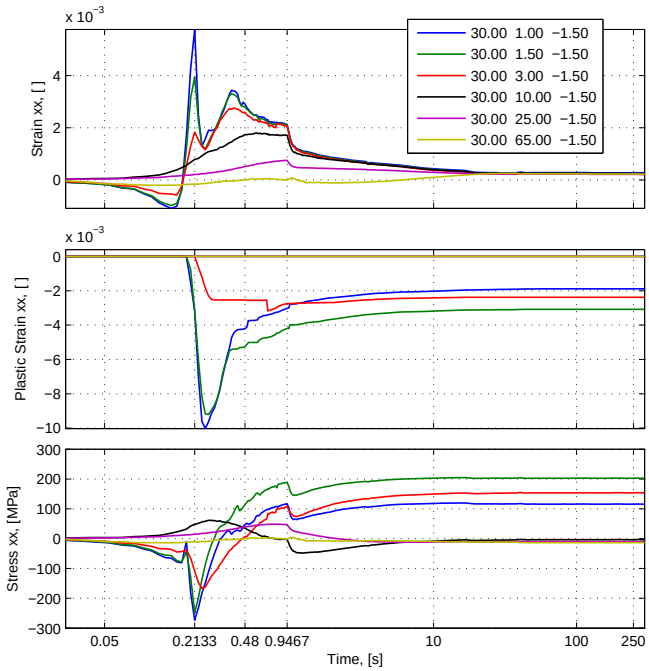

Figure 16: History of longitudinal strain and stress for points of the form (30, y, −1.5).

and reach maximum values for points close to the welding line. This shows the transference of the mechanical effects, while the thermal strain affects other locations than the observed ones.

Contrary to this, the plastic strain only appears when the high temperature gradients and values of strain occur. In other words, if the laser beam would never reach the coordinate $x = 30$mm, the deformations will disappear inmediately after the loads (thermal or mechanical) are removed.

The plastic strain changes only in size as the material cools down, but remains different from zero forever, even though the temperature distribution returns to a homogeneous state. This is due to the fact that only high temperature changes can produce a thermal strain for which the corresponding stress is outside the yield point for an elastic behavior.

The stress evolution can be observed to be the result of the combination of strain and plastic strain, and it is interesting to see how the stabilization of its values takes place only after the material is released from new heat inputs and cools down. The only release of the material from the heat input does not finish the strain and stress evolution. This is why the simulation of the cooling stage is

very important.

It is also possible to observe some jumps during the stabilization process before the weld ends. This is the result of the cooling process, as during this time the material suffers a decrease in temperature from its melting point to about 250 °C, which is also the temperature intervals where most of the material properties have large changes.

As an example of such changes in the material properties, the yielding stress σ_Y used for the simulations has a value of about 200 MPa at 250 °C and is decreased to 40 MPa at 600 °C. More details about this changes, can be seen from the material properties in [15].

Figure 17 presents similar plots to the ones in the previous figure, but for points located along the traversal line with coordinate $x = 50$mm.

The behavior in Figures 16 and 17 is very similar. There are two main things where a difference can be observed, namely the periods at which each phenomenon occur, and the extreme values obtained at the moment of highest temperature.

The differences in the extreme values are due to the different geometric lo-

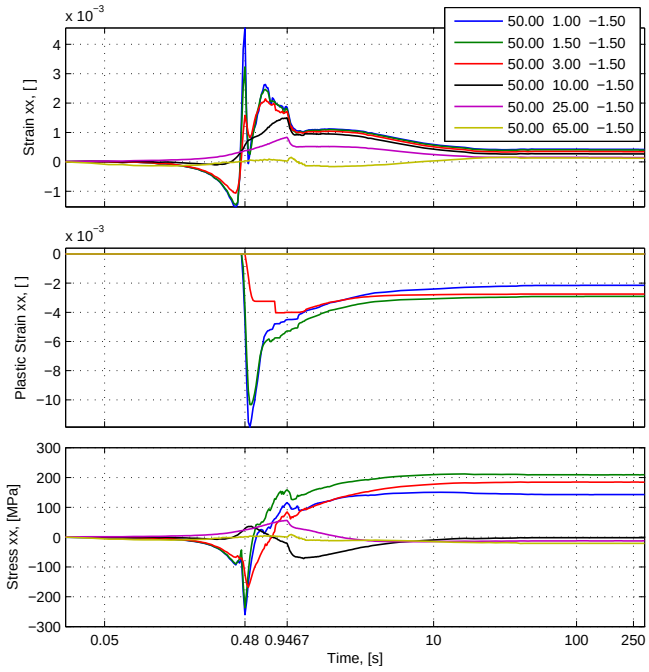

Figure 17: History of longitudinal strain and stress for points of the form (50, y, −1.5).

cation of the measuring points. Points belonging to the middle of the plate are more restricted to move and present a higher plastic strain. The size of the plastic strains can be observed to be larger for the points at $x = 50$ mm, compared to the ones at $x = 30$ mm. The opposite can be observed for the strains.

The overall process shown in Figure 17 repeats the behavior for the new coordinate $x = 50$mm, and every plot has a shape similar to the corresponding plot in Figure 16, changing only the times at which the single changes occur.

In Figure 17, the time where the maximum effects occur in the new plots equals the middle of the welding time. However, the stabilization part is qualitatively the same, and the final values are also very similar. This is then reflected in the residual equivalent stress shown in Figure 15.

It is important to remark that Figures 16 and 17 present only the plots for the longitudinal component, which is the common way to analyze the mechanical behavior in the computational welding mechanics community.

Although the plots containing all the components could have also been considered, the amount of components and different locations would make any attempt of analysis very confusing. See [15] for an example of such analysis.

The specifications in Table 3 show the computational expenses to get the results presented before, including all numerical computation time from the keyhole formation to the mechanical calculation during the cooling time and the measurements of the residual stresses and deformation angle.

Additionally, Table 4 contains the characterizing numbers for the simulated weld. In this table, the value assigned as equivalent stress corresponds to the L^2-norm of the equivalent stress over the whole plate at the end of the simulation ($t = t_w + t_{cool}T$), divided by the piece volume.

Processor: AMD-Athlon 64 Dual-Core, 2.0GHz
Installed RAM: 2.0GB
Total computation time: 2.67 hrs. (100%)
Computation time for welding: 2.18 hrs. (82%)
Minimum system DOFs: 8364
Maximum system DOFs: 21295
Number of time steps: 272

Table 3: Summary of computational expenses

	Simulated	Experimental
Laser power (P)	3000 W	3000 W
Welding velocity (v)	75 mm/s	75 mm/s
Meltpool top width w	2.657 mm	2.06 – 2.15mm
Meltpool height h	1.958 mm	1.92 – 2.30mm
Equivalent stress at T	0.584 MPa	
Out-of-plane angle	0.9520°	1.003°

Table 4: Main simulation results

6. Discussion

The overall process of the laser welding process includes many physical effects and, consequently, many process variables are needed to obtain a significant model. The modeling proposed here is not the first for the laser welding application, but includes several features that have not been used in combination for this kind of applied process.

6.1. Approximation of thermal fields

The efficient simulation of the thermal problem was attained very well, considering the obtained general shapes of thermal fields, and the numerical quantification of the molten region sizes and their comparison with experimental data. In addition to the comparisons presented in Section 5, there are other examples of successful simulation–experimental comparisons of our model in [21] and [15].

Regardless of the very simple and fast way of constructing the keyhole and assign its shape to the heat source, this approximation allows a computation of the thermal fields with enough precision. However, it must be also said that the approach used in this work is not suited for a detailed simulation of the complete keyhole dynamics.

Furthermore, it is remarkable the good results of simulating with an adaptive procedure, making the large computational expenses to be taken in the areas of higher thermal changes, while producing a lose resolution in other less important areas.

However, attention must be paid to the corresponding adaptivity tolerance, which controls the level of refinement and its selection is not a trivial task. A slightly small tolerance can result in a high refined mesh, slowing down the simulation, while a large tolerance can lose the necessary refinement level in the heat input areas. Different material sizes and geometries can also require very different tolerances.

6.2. Mechanical calculations

The high strains created during the welding process lead to permanent deformations and thus the use of a plastic solver is necessary. To solve the plastic problem, the radial return mapping was successfully implemented for the computation of residual strains and stresses on the material.

As shown in Section 5, the deformation computed using our elasto-plastic implementation leads to good results when compared with the experimental measurements for the deformation.

Based in the existent computational welding mechanics literature, the computed stress tensor behaves as expected, and the plastic zones due to the welding temperature gradients can be well identified.

The residual deformation was measured and also used to determine the experimental deformation angle. A good accordance between experimental and simulated out-of-plane angles was also achieved.

However, in order to better calibrate the mechanical model, a precise measurement of the displacement during the welding process or of the stress in the residual stress would be necessary.

Practical experience with the simulation code has shown that the size of the elements around the welding line, the symmetry of the mesh to both sides of this line, as well as the cut-off temperature used for the material properties, influence the mechanical results in a complicated manner. A detailed study of their single influences has not been done until now.

7. Conclusion and prospects

The results of the welding simulations can be considered in general as very efficient and realistic, but also as expandable and with large possibilities of enhancement.

After an experimental comparison, it can be said that the simulation purposes have been achieved and that this model can be used to simulate the welding process within a practical range of process parameters.

The implemented methods allow their use into similar tasks. Examples of it are the diverse thermal driven joining techniques, thermal forming applications, or mechanical load and unload processes, among others.

It must be also said that the modular ALBERTA implementation allows for expansions in a natural way, making possible a future inclusion of new ingredients into the model, as could be the computations for the liquid motion, the use of different error estimators, or other mechanical solvers.

Furthermore, it is important to remark that ALBERTA is an open source toolbox and that all our implementations are self contained and independent of any kind of commercial software.

Although the simulations have been successfully carried out, there are still some open questions, like the way of best selecting the adaptive tolerance or the real effects of the liquid convection.

Further ideas to improve the simulated welds are to include the fluid dynamic computations for the meltpool, to include a hot-crack prediction submodel, or to use different material parameters for each of the welded pieces.

Acknowledgements

The authors thank to the ZF of the Universität Bremen and to the CONACYT-Mexico for the financial Support.

References

[1] W. M. Steen, J. Dowden, P. Kapadia, A point and line source model of laser keyhole welding, J. Phys D: Appl. Phys. 21 (1988) 1255–1260.

[2] D. Radaj, Eigenspannungen und Verzug beim Schweissen: Rechen- und Messverfahren, Vol. 143 of Schweisstechnik, DVS: Verlag fuer Schweissen und Verwandte Verfahren, 2002.

[3] W. Jüptner, Untersuchungen zum einbrandverhalten eines elektronenstrahls unter berücksichtigung der strahlgeometrie, Ph.D. thesis, Fakultät für Maschinenwesen der Technischen Universität Hannover (1975).

[4] A. Kaplan, A model of deep penetration laser welding based on calculation of the keyhole profile, J. Phys. D: Appl. Phys. 27 (1994) 1805–1814.

[5] J. Trappe, J. Kroos, C. Tix, G. Simon, On the shape and location of the keyhole in penetration laser welding, J. Phys. D: Appl. Phys. 27 (1994) 2152–2154.

[6] P. Solana, J. L. Ocaña, A mathematical model for penetration laser welding as free-boundary problem, J. Phys. D: Appl. Phys. 30.

[7] H. Ki, P. S. Mohanty, J. Mazumder, Modeling of laser keyhole welding: Part I. Mathematical modeling, numerical methodology and role of recoil pressure, multiple reflections, and free surface evolution, Metallurgical and Materials Transactions A 33A (6) (2002) 1817–1830.

[8] W. Jüptner, T. Kreis, Mathematisches Model zur Beschreibung der Wechselwirkung zwischen Strahlen hoher Intensität und technischen Werkstoffen, Forschungsbericht, Bremer Institut für angewandte Strahltechnik (1982).

[9] R. Rothe, Beispielsrechnung für konstante, gaussförmige und ringförmige Verteilung der Leistungsdicht für gleiche Parameter, unpublished.

[10] A. Schmidt, K. G. Siebert, Design of Adaptive Finite Element Software: The Finite Element Toolbox ALBERTA, Springer, 2005.

[11] U. Dilthey, Schweisstechnische Fertigungsverfahren, 3rd Edition, Vol. 2: Verhalten der Werkstoffe beim Schweissen, Springer, 2005.

[12] J. A. Goldak, M. Akhlaghi, Computational Welding Mechanics, Springer, 2005.
[13] F. Vollertsen, G. Habedank, Schweisstechnische und verwandte Verfahren 1, Lecture notes, University of Bremen (2004).
[14] J. C. Simo, T. J. R. Huges, Computational Inelasticity, Springer, 1999.
[15] J. Montalvo-Urquizo, Simulation and Optimization of Laser Welding on Aluminum Alloys, Ingenieurwissenschaften, Dr Hut Verlag, München, 2008.
[16] W. Han, B. D. Reddy, Plasticity: Mathematical theory and numerical analysis, Springer, 1999.
[17] C. Wieners, Theorie und Numerik der Prandtl-Reuss-Plastizität, Hablitation Tesis, Universität Stuttgart (1999).
[18] A. Geilenkothen, Efficient solvers and error estimators for a mixed method in elastoplasticity, Ph.D. thesis, Fachbereich Mathematik, Universität Hannover (2004).
[19] C. Wieners, Nonlinear solution methods for infinitesimal perfect plasticity, Z. Angew. Math. Mech. 87 (8–9) (2007) 643–660.
[20] D. Radaj, Heat effects of welding: temperature field, residual stress, distortion, Springer, 1992.
[21] Z. Akbay, J. Montalvo-Urquizo, T. Pretorius, F. Vollertsen, Fast FEM-Model and Keyhole-Heat Source Model for Self-Optimized Simulation of Laser Welding Processes, in: F. Vollertsen, J. Sakkiettibutra (Eds.), Thermal Forming and Welding Distortion: Proceedings of the International Workshop on Thermal Forming and Welding Distortion, BIAS, 2008, pp. 277–288.